Materials Today Bio 18 (2023) 100535

Contents lists available at ScienceDirect

Materials Today Bio

journal homepage: www.journals.elsevier.com/materials-today-bio

Core-shell oxygen-releasing fibers for annulus fibrosus repair in the intervertebral disc of rats

Yi Zheng [a,1], Borui Xue [a,1], Bin Wei [a,1], Bing Xia [a], Shengyou Li [a], Xue Gao [a], Yiming Hao [a], Yitao Wei [a], Lingli Guo [a], Haining Wu [a], Yujie Yang [a], Xueli Gao [b], Beibei Yu [c], Yongfeng Zhang [c], Shijie Yang [c], Zhuojing Luo [a,***], Teng Ma [a,d,**], Jinghui Huang [a,*]

[a] Department of Orthopedics, Xijing Hospital, The Fourth Military Medical University, Xi'an, 710032, China
[b] School of Ecology and Environment, Northwestern Polytechnical University, Xi'an, 710072, China
[c] Department of Neurosurgery, The Second Affiliated Hospital of Xi'an Jiao Tong University, Xi'an, 710004, China
[d] Military Medical Innovation Center, The Fourth Military Medical University, Xi'an, 710032, China

ARTICLE INFO

Keywords:
Perfluorotributylamine
Coaxial electrospinning
Annulus fibrosus defect
Intervertebral disc degeneration
Hypoxia

ABSTRACT

The repair of annulus fibrosus (AF) defect after discectomy in the intervertebral disc (IVD) has presented a challenge over the past decade. Hostile microenvironments in the IVD, including, compression and hypoxia, are critical issues that require special attention. Till date, little information is available on potential strategies to cope with the hypoxia dilemma in AF defect sites. In this study, perfluorotributylamine (PFTBA) core-shell fibers were fabricated by coaxial electrospinning to construct oxygen-releasing scaffold for promoting endogenous repair in the AF after discectomy. We demonstrated that PFTBA fibers (10% chitosan, chitosan: PCL, 1:6) could release oxygen for up to 144 h. The oxygen released from PFTBA fibers was found to protect annulus fibrosus stem cells (AFSCs) from hypoxia-induced apoptosis. In addition, the PFTBA fibers were able to promote proliferation, migration and extracellular matrix (ECM) production in AFSCs under hypoxia, highlighting their therapeutic potential in AF defect repair. Subsequent *in vivo* studies demonstrated that oxygen-supplying fibers were capable of ameliorating disc degeneration after discectomy, which was evidenced by improved disc height and morphological integrity in rats with the oxygen-releasing scaffolds. Further transcriptome analysis indicated that differential expression genes (DEGs) were enriched in "oxygen transport" and "angiogenesis", which likely contributed to their beneficial effect on endogenous AF regeneration. In summary, the oxygen-releasing scaffold provides novel insights into the oxygen regulation by bioactive materials and raises the therapeutic possibility of oxygen supply strategies for defect repair in AF, as well as other aerobic tissues.

1. Introduction

Low back pain is a global public health concern, and anywhere between 75 and 80% of people suffer from back pain at any point in their lives [1]. Intervertebral disc (IVD) degeneration is the largest contributor of back and neck pain [2,3]. During early degeneration, the IVD undergoes extracellular matrix (ECM) loss in the nucleus pulposus (NP) tissue, causing alterations in osmotic pressure and the structure of the collagen fibers in the annulus fibrosus (AF), thus, leading to the occurrence of IVD herniation, which, in turn, remodels the composition, structure and mechanical properties of the disc, thereby accelerating IVD degeneration [4]. Currently, discectomy (removal of the herniated NP tissue) can effectively relieve IVD herniation symptoms, but it usually leaves a large defect in the AF tissue [5]. Current researches suggest that untreated AF defect typically induces further degeneration within 6 weeks, including loss of NP tissue hydration, persistent lesions within the fibrous structure in AF tissue, NP re-herniation, and reduced IVD function [6–8].

There is a clear clinical need for AF defect repair after discectomy, however, clinical treatment has been relatively stagnant over the past

* Corresponding author. Department of Orthopedics, Xijing Hospital, The Fourth Military Medical University, 710032, Xi'an, China.
** Corresponding author. Department of Orthopedics, Xijing Hospital, The Fourth Military Medical University, 710032, Xi'an, China.
*** Corresponding author. Department of Orthopedics, Xijing Hospital, The Fourth Military Medical University, 710032, Xi'an, China.
E-mail addresses: zhuojingl@163.com (Z. Luo), mateng_cn@foxmail.com (T. Ma), huangjh@fmmu.edu.cn (J. Huang).
[1] These authors contributed equally to this work.

https://doi.org/10.1016/j.mtbio.2022.100535
Received 12 September 2022; Received in revised form 15 December 2022; Accepted 26 December 2022
Available online 3 January 2023

decade [9,10]. AF defect repair is a complex process that undergoes acute inflammation, endogenous annulus fibrosus stem cells (AFSCs) proliferation, and fiber remodeling [11]. In contrast to the poorly vascularized zones in the central NP tissue, vascularization plays a more crucial role in AF. During fetal development, blood vessels are significantly located deep within the AF to provide sufficient nutrient supply to the growth and development of the IVD [12,13]. However, during postnatal growth, the blood vessels recede and localize around the AF tissues, which limits the supply of nutrients (such as oxygen) to the IVD [14]. In addition, endogenous cells increase their metabolic oxygen consumption as they degenerate, consequently aggravating the local hypoxia prior to revascularization in the regenerated AF [15]. Therefore, in contrast to the avascular NP tissue, the hypoxia role should be given more attention during AF regeneration. In the past few decades, biomaterials and tissue engineering strategies have revealed the potential to repair AF defects, however, studies suggested that the function of AF bioengineered implants may be, at least in part, limited by the local hypoxic environment [16–20]. Till date, little information is available on the strategies for oxygen delivery in AF defect sites.

Perfluorotributylamine (PFTBA) is a perfluorocarbon with high oxygen solubility [21]. In addition, PFTBA is also an oxygen carrier with biological inertness and good histocompatibility [22]. Recently, studies confirmed the potential of PFTBA as a source of oxygen delivery in the repair of osteochondral and peripheral nerves, which aids in overcoming the hypoxic environment at the injury site, thereby accelerating tissue repair [23–25]. In a previous study, we have demonstrated that PFTBA-enriched alginate scaffolds promote NP cell survival, proliferation and ECM expression, which ultimately alleviates IVD degeneration [26]. Therefore, the PFTBA-based system holds the potential of delivering oxygen during AF defect repair. In view of the completely different structural properties from gel-like NP tissue, the materials for repairing AF defects requires good mechanical strength, to withstand the internal pressure and radial stress of the IVD tissue [27]. Electrospinning has unparalleled advantages during AF repair and regeneration due to its high aspect ratio and good mechanical properties such as stress-strain and elastic modulus [28–30]. Moreover, elevated porosity and large pore size in fiber-based scaffold enables cells to migrate, infiltrate, and grow into the scaffolds, which provides favorable conditions for cell adhesion and growth [28]. In addition, additives can be loaded *via* numerous nanofibrous structures to improve tissue regeneration properties, making electrospinning attractive for oxygen delivery during AF repair [31].

In this study, we employed the coaxial electrospinning technique to fabricate core-shell fibers. Firstly, PCL was selected as the shell structure for coaxial electrospinning fibers, as it is soluble in organic solvents and has been widely studied in the IVD repair, owing to its suitable mechanical properties [28,32]. Secondly, chitosan was employed as the core structure as PFTBA is dissolvable in chitosan aqueous solution, and can aid in oxygen delivery. We characterized the oxygen release kinetics of PFTBA coaxial electrospinning fibers, and then investigated the effects of PFTBA core-shell fibers on cell viability, proliferation, migration and ECM production of AFSCs *in vitro*. Furthermore, the efficacy of PFTBA fibers on IVD repair was assessed *in vivo* using combinations of radiographic, histological and molecular studies (Scheme 1).

2. Materials and method

2.1. PFTBA coaxial electrospinning fibers fabrication

2.1.1. Core and shell solutions preparation

The PFTBA core solution preparation was carried out in accordance with previous investigations [33]. Briefly, 190 mg of egg yolk lecithin (Sigma, USA) was dissolved in 1 mL of Tyrode's solution (Sigma, USA), and mixed *via* ultrasonic shaker twice at 4 °C for 15 s. Subsequently, 1 mL of PFTBA stock solution was introduced, followed by sonic concussion 10 times under the same parameters. In control groups (without PFTBA), PBS (Gibco, USA) was introduced instead. Finally, carboxyl-chitosan (Sigma, USA) was introduced to the above emulsion to form a gelatinized core solution. Varying concentrations of carboxyl chitosan (5% w/v, 7.5% w/v, 10% w/v, 12.5% w/v, 15% w/v; 20% w/v, Sigma, USA) were used to form the optimal structure. In addition, to prepare the shell solution, 20% w/v polycaprolactone (PCL, Sigma, USA) particles were dissolved in methanol-chloroform solution, in a 1:4 v/v ratio. To observe the electrospinning process, Rhodamine B (1 mg/mL, Sigma, USA) was mixed with the shell material, fluorescein isothiocyanate (FITC; 2 mg/mL, YEASEN, China) with the core material, and the core-shell structure was fluorescently labeled during the electrospinning process.

2.1.2. Electrospinning of core-shell structures

A coaxial spinneret (inner diameter 0.3 mm, outer diameter 1.2 mm) was employed, and the core and shell materials were extracted with a 10 mL syringe, and connected to the inner and outer tubes of the spinneret (Scheme 1A). The shell injection speed was 0.6 mL/h, and the core injection speed was 0.06–0.15 mL/h, and the speed was controlled by syringe pumps (LSP02-1B, Longer, China). A high-voltage power supply (Donwen, China) was applied at the spinneret. To fabricate fiber membranes, a metal plate was used to receive fibers. Electrospinning process was pictured using a digital camera (X100f, Fujifilm, Japan). Fluorescence microscope (DM6000, Leica, Wetzlar, Germany) was used to observe the core-shell structure. Scanning electron microscopy (SEM, JSM-4800; HITACHI, Japan) was employed to observe the spinning material structure. Moreover, the nitrogen adsorption-desorption analysis instrument (ASAP 2460, Micrometrics, USA) was used to analyze the Brunauer-Emmett-Teller (BET) specific surface area.

2.2. Oxygen release behavior detection

To evaluate the oxygen releasing capacity of the PFTBA core-shell structure, fiber membranes with or without PFTBA were sliced into a 15.6 mm diameter circular membrane, and inserted into a 24-well plate (Thermo, USA) with 1 mL of serum-free DMEM/F12 medium (Gibco, USA) per well. The plate was then placed in a normal oxygen incubator or hypoxic incubator (0.5% O_2/5% CO_2). At each time point, a blood gas analyzer (Bayer, Germany) was employed for medium oxygen level detection.

2.3. In vitro analysis

2.3.1. Isolation, identification, and culture of AFSCs

AFSCs were isolated from the tail IVD of 8-week-old Sprague Dawley (SD) rats, as previously described, followed the animal care guidelines approved by the Animal Research Committee of the Fourth Military Medical University [32,34,35]. Briefly, after euthanasia, rat tails were harvested and soaked in ice alcohol for 10 min and then were transferred to a sterile environment. Next, they were cut through the skin and tendon tissue to expose the disc. Upon removal of the NP tissue, the AF tissue was minced into 1 × 1 × 1 mm pieces, and digested with trypsin (0.03%, Sigma, USA) and type I collagenase (1 mg/mL; Sigma, USA) for 1h. The resulting suspension was then centrifuged at 1000 rpm for 5 min, and resuspended in DMEM/F12 (1:1) medium (containing 10% FBS, 1% Penicillin/Streptomycin), prior to incubation at 37 °C with 5% CO_2. Following 24 h of incubation, suspended cells were removed by replacing old medium with fresh DMEM/F12 (1:1) medium. The adherent cells were cultured for another 3–5 days, and passed when the cell density reached 90%. The collected primary cells were cultured at a density of 1 × 10^3 cells/ml, under which stem cells can form colony-forming units, whereas mature AF cells do not. After 10 days, trypsin was used locally to extract colony cells, which were subsequently cultured for the first passage AFSCs. Cells belonging to the 4–6 passage were used for experimentation to make sure the purity of AFSCs. Cells were treated with antibodies (CD29, CD90, CD105, CD34, CD45; Invitrogen, USA) prior to flow cytometry (FCM) identification. Moreover, using osteogenic

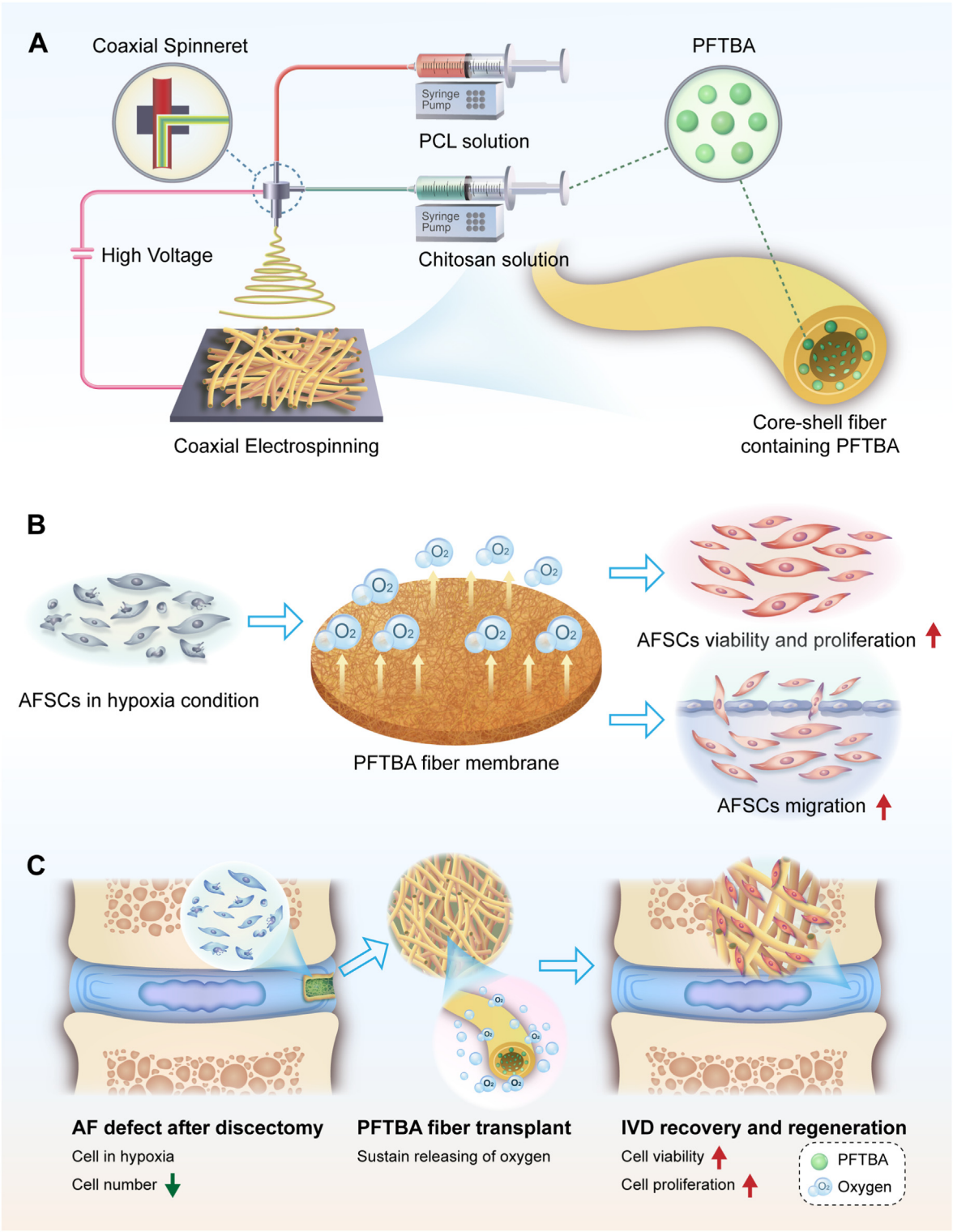

Scheme 1. (A) A schematic illustration of the electrospinning process of core-shell fibers. (B) Effects of PFTBA oxygen-supplying fibers on the survival and function of AFSCs. (C) Application of the PFTBA core-shell scaffold in repair of AF defect after discectomy.

(GUXMX-90021, Cyagen, China), adipogenic (GUXMX-90031, Cyagen, China) and chondrogenic differentiation induction media (GUXMX-90041, Cyagen, China), we examined the osteogenic, adipogenic and chondrogenic differentiation abilities of AFSCs *via* alizarin red, oil red O and alcian blue staining. Relative gene expressions were quantitatively analyzed *via* qPCR. The primers are listed in Table 1. Lastly, to assess *in vivo* differentiation of AFSCs, 5×10^5 cells were transplanted into the subcapsular region of immune-deficient mice, and the kidneys were frozen-sectioned after 8 weeks for staining with Safranin O-Fast Green (SOFG) stain.

2.3.2. Viability and proliferation examinations

After sterilization by ^{60}Co irradiation, PFTBA electrospinning membranes were tiled on the bottom of a 24-well plate (Thermo, USA). Then,

Table 1
Primers used for qPCR.

Primer	Sequence (forward 5′-3′)	Sequence (reverse 5′-3′)
COL2A1	GTGGACATAGGGCCTGTCTG	CCGGACTGTGAGGTTAGGAT
SOX9	CCAGACCCTGAGGAGACCTT	CTCCTGGAATCTCAGCAATCGT
PPARG	TTCGCTGATGCACTGCCTAT	GTCAGCTCTTGTGAACGGGA
ADIPOQ	TGTCTGTACGAGTGCCAGTG	CCCGGTATCCCATTGTGACC
RUNX2	AGCAGACCGTCAAAGGTGTT	CTCTCGTCCCTTTCCGAGTG
SP7	AGGTCCTGGCAACACTCCTA	CAGACGGGTAAGTAGGCAGC
COL1A1	GGGACACAGAGGTTTCAGTGG	CACCGACAGCACCATCGTT
COL3A1	CCTGGACCAGCAGGAGCTAAT	TGGTGACCCATCTTTGCCG
HOXB9	AGGGAGGCTGTCCTGTCTAAT	CAGAGGGGTTGGTTTGATCC
NOD2	CTAGAGGAGCTCTGACTCCAAG	CACTGACCCCCATCAGAACC
CDH13	GCCGGTCCTAAACTTGACCT	ACAGCCACTAAGGTGCCATC
ADAMTS3	GAACGCCCAGGAAACTTGGGTA	AAGAACATGAGGAGAAGCCTCG
PLXNA4	GGCGCTCACCATCCTACATT	AGGTGTGTTCCCACTGACAA
GAPDH	GGCACAGTCAAGGCTFAGAATG	GGTGGTGAAGACGCCAGTA

AFSCs were seeded on the membranes at a density of 1×10^5 cells/mL. As control, cells were seeded on electrospinning membranes without PFTBA. The aforementioned cells were then placed in a normoxic or hypoxic incubator, and cell viability was detected *via* FCM at 48 h, 96 h and 144 h. Cell proliferation was assessed by CCK-8 assay, and cell counts *via* Phalloidin and DAPI staining. The cell spread on membrane was observed *via* SEM.

2.3.3. Transcriptome analysis

Following RNA isolation using Gene Denovo Biotechnology Co. (Guangzhou, China), NGS sequencing and data analyses were performed. Subsequently, differential transcript expression analysis was performed using the R package DEseq2. Differentially expressed RNAs with $|\log2(FC)| > 1$ and q-values <0.05 were considered significant differential expression genes (DEGs). Pathway and GO enrichment analyses were performed using the KEGG (http://www.genome.ad.jp/kegg) and GO databases. FDR correction was done on the calculated *p* values, with FDR ≤ 0.05 as the threshold. Lastly, gene set enrichment analysis was performed using the GSEA and MSigDB software, and enrichment scores with *p* values and default parameters were computed.

2.3.4. Immunofluorescence

Cells were fixed in 4% paraformaldehyde, prior to infiltration with 0.2% Triton X-100 for 20 min. Next, cells were blocked in 10% normal goat serum for 1 h at room temperature (RT), with subsequent incubation with antibodies (anti-collagen I (1:200) and anti-collagen III (1:200)) for 12 h at 4 °C, then with secondary antibody (FITC or Cy-3, 1:200) for 1 h at RT, prior to nuclear staining with DAPI. Cells were observed under a fluorescence microscope, and quantitatively analyzed with the ImageJ software (NIH, USA).

2.3.5. Real-time PCR assay

Total RNA was extracted from AFSCs following the Total RNA Kit (QIAGEN, Germany) directions, then reversed to cDNA using SYBR Green PCR Master Mix (TAKARA, China). Finally, qRT-PCR was conducted and analyzed *via* a BioRad CFX96 PCR System (BioRad, Australia). The primers are listed in Table 1.

2.3.6. Transwell experiments

To examine the effects of PFTBA on cell migration, electrospinning membranes with or without PFTBA were placed in 6-well transwell chambers (pore size: 8 μm, NUCN, Denmark). In addition, 1×10^5 cells were seeded on the upper chamber of the transwell filter. Subsequently, 2 mL of medium was introduced to the transwell chamber, and cells were placed in normoxic and hypoxic incubators, respectively. After 24 h of incubation, cells remaining on the top of the filter were removed, and those that migrated to the lower surface were fixed with 4% paraformaldehyde, prior to crystal violet staining, finally analyzed under a microscope (BX53F, Olympus).

2.4. In vivo experiments

2.4.1. Animals and surgical procedure

All animal experiments followed the animal care guidelines approved by the Animal Research Committee of the Fourth Military Medical University (License no. IACUC-20220130). Male SD rats (3-month-old, N = 32) were arbitrarily divided into 4 groups: Control, Defect, Fiber, and PFTBA groups. The control group had no AF defect. The defect group experienced AF defect, which was left untreated. The other two groups received fiber implants after AF defect, and the PFTBA group received fibers containing PFTBA. Under general anesthesia, a 1 cm longitudinal incision was made along the tail in sterile environment to expose the caudal IVD (Co5–Co6). Next, a 2×0.5 mm defect, approximately 0.5 mm deep, was generated in the AF tissue under a microscope. Subsequently, for the treatment groups, fibers with or without PFTBA were implanted at the defect site and glued on with medical adhesive (Baiyun medical adhesive, Guangzhou, China). X-rays and magnetic resonance imaging (MRI) were performed at 2, 4 and 8 weeks post operation. After 8 weeks, the rats were euthanized. Co5–Co6 discs were resected for subsequent analysis. Preparation of transcriptome analysis was according to the aforementioned methods.

2.4.2. X-ray

The X-ray imaging of rat tail vertebrae was performed at 2, 4 and 8 weeks post operation, using an X-ray system (Faxitron Biooptics LLC, Wheeling, IL, USA). The IVD Height Index (DHI) was measured using the method described previously [36]. Alterations in DHI are expressed in % DHI.

2.4.3. MRI

MRI imaging was performed at 2, 4 and 8 weeks post operation, using an MRI system (Siemens 3T Magnetom Trio Tim Scanner, Munich, Germany). Two blinded doctors computed the degeneration score, based on the Pfirrmann grading system, ranging from 1 to 5 points, as previously described [37].

2.4.4. Micro-CT

A Micro-CT system (eXplore Locus SP; GE, Fairfield, USA) was used to scan the sample with a voltage of 80 kV, current of 80 mA, and exposure time of 3000 ms, using specific parameters (resolution 14 mm, voxels 27 mm and threshold 1150). 3D images were reconstructed using the Microview v1.1.1 software (GE Medical Systems, USA). The bone volume/tissue volume (BV/TV) of the upper and lower end plates of each IVD were then calculated.

2.4.5. Histological assessment

For staining, IVD tissues were fixed in 4% paraformaldehyde, prior to decalcification with 10% EDTA (PH 7.4) for 2 months before sectioning. Then, samples were transferred to 75% ethanol, embedded in paraffin, and cut into 7 μm thick sagittal sections. The sections were then stained with Safranin O-Fast Green (SOFG), Sirius red, hematoxylin and eosin (H&E). Staining samples were imaged with a bright field microscope, and the Sirius red staining was analyzed for collagen imaging under polarized light. The histological scores were assessed by two independent, uninformed investigators. Anti-CD34 (Abcam, USA), Anti-FSP1 (CST, USA) and Anti COL1 (Abcam, USA) antibodies were used for immunofluorescence staining, prior to observation under a fluorescence microscope, and finally quantitatively analyzed with the ImageJ software. For SEM scanning, IVD tissues were cut in a mid-axial direction, and fixed in 2.5% glutaraldehyde for 24 h. Then, tissues were sputter coated with gold after dried under partial vacuum, and observed under SEM (voltage: 5–10 kV).

2.5. Statistical analysis

The experimental data are provided as mean ± SD, and compared using one-way ANOVA followed by the Bonferroni test *via* SPSS.20

software. $p < 0.05$ was considered statistically significant.

3. Results

3.1. Fabrication and optimization of PFTBA core-shell fibers

The fibers with PFTBA core-shell structure were prepared using coaxial electrospinning (voltage: 15.5 kV). Firstly, we prepared core-shell structures containing PFTBA, according to the parameters in Fig. 1A. During the parameter screening process, we demonstrated that the coaxial fiber formation process was stable when the chitosan concentration was increased to 7.5%, and the chitosan: PCL was decreased to 1:10 (Fig. 1B). When the chitosan concentration was increased to 20%, the core solution intermittently cut off the shell solution supply, thus, resulting in the instability of the core-shell structure. By adjusting PCL to chitosan ratio and the concentration of chitosan, we finally identified 5 sets of parameters that formed the core-shell structure. As illustrated in Fig. 1C, we introduced fluorescent dyes Rhodamine B to the shell and FITC to the core solution, and the structure was identified *via* fluorescence microscopy, showing red in the shell and green in the core. Those

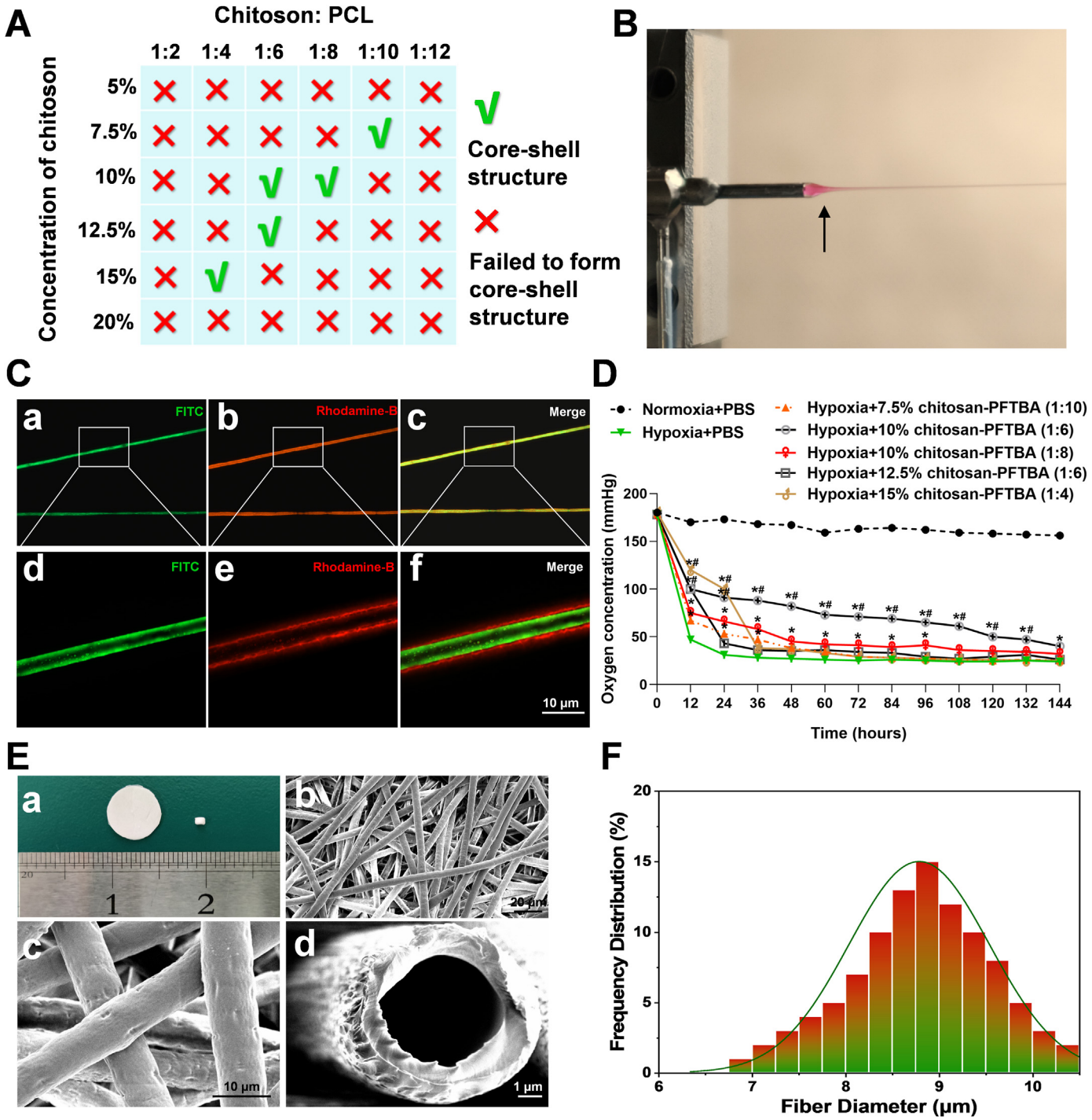

Fig. 1. Preparation and optimization of the coaxial electrospinning fibers. (A) Parameter screening of the core-shell structure. (B) Formation of the core-shell structure. (C) Observation of the core-shell structure under fluorescence microscopy. (D) Oxygen release behavior. (E) Microstructure of fibers under scanning electron microscopy. (F) Distribution of fiber diameters. $^{*}p < 0.05$ *vs.* Hypoxia + PBS group, $^{\#}p < 0.05$ *vs.* Hypoxia +7.5% chitosan-PFTBA group.

results verified the successful construction of the core-shell structure.

To further screen the optimal parameters for PFTBA to release oxygen in the core-shell structure, we evaluated the oxygen release characteristics of the PFTBA core-shell structure fibers. In the core-shell structure without PFTBA, the oxygen level of the surrounding medium did not exceed 50 mmHg at 12 h of hypoxic treatment. When PFTBA was present in the core-shell structure, the oxygen level of the surrounding medium was significantly increased. A burst release of oxygen was observed in 12.5% and 15% chitosan-PFTBA groups for 36 h (Fig. 1D). Moreover, in the 10% chitosan-PFTBA group (chitosan: PCL, 1:6), we found significantly higher oxygen level in the medium under hypoxia for 36–144 h than the other chitosan-PFTBA fibers. Following hypoxic treatment for 144 h, the oxygen in fibers were exhausted and the oxygen content in each group was sustained at low levels. Then SEM was further employed to characterize the fiber microstructure (10% chitosan, chitosan: PCL, 1:6, Fig. 1E). It was revealed that the core-shell fibers were randomly distributed within the fiber membrane, and the core-shell structure was visible at the cross section of the fiber (Fig. 1E). Moreover, the fiber diameters ranged from 6.75 to 10.5 μm, with a mean diameter of 8.75 μm (Fig. 1F). Additionally, the nitrogen adsorption-desorption analysis was conducted to examine the specific surface area. The isotherms of nitrogen adsorption-desorption of PFTBA fibers are presented in Fig. S1, and the specific surface area calculated from the nitrogen adsorption was 18.0533 m^2/g. Therefore, we employed the aforementioned parameters (10% chitosan, chitosan: PCL, 1:6) to prepare and construct the PFTBA core-shell fiber materials for AF defect repair in the remainder of the present study.

3.2. Isolation and identification of AFSCs

During primary culture, several cell types were present in culture dish, but mostly elongated AF cells (Fig. S2A). In separate culture, AFSCs colonies were numerously presented after 10 days of culture (Fig. S2B), and AFSCs presented polygonal, spindle-shaped or cobblestone-shaped (Fig. S2C). The cell colonies were then harvested by local application of trypsin under microscopy to obtain AFSCs. The AFSCs in the present study highly expressed typical mesenchymal stromal (MSC)cell markers CD29, CD90, and CD105, but not hematopoietic markers CD34 and CD45 (Fig. 2A), which was in line with previous reports [38,39]. Next, the multi-directional differentiation potential was identified after induction of adipogenic, osteogenic, and chondrogenic differentiation (Fig. 2B–D). The differentiation efficiency was further quantified using quantitative real-time PCR (qPCR) analysis. The marker genes for adipogenesis (ADIPOQ and PPARG), osteogenesis (RUNX2 and SP7), and chondrogenesis (SOX9 and COL2A1) in the induced groups were higher than in the control group (Fig. 2E). To further test the *in vivo* differentiation potential of AFSCs without induction or away from the IVD microenvironment, we performed renal capsule transplantation of AFSCs in immunodeficient mice (Fig. 2F). Eight weeks post transplantation, SOFG staining revealed that the AFSC differentiated into fibroblast-like cells similar to renal capsule membrane phenotype without *in vivo* induction, but not into chondrocyte-like cells (red color in SOFG stain, Fig. 2F). These results confirmed the identity of the isolated AFSCs.

3.3. The PFTBA core-shell fibers protect AFSCs against hypoxia in vitro

To evaluate the AFSCs activity on PFTBA core-shell fiber membrane, we used FCM to analyze cell apoptosis of in each group under hypoxic conditions (Fig. 3A–D). At 48 h, 96 h and 144 h, no significant difference was observed in the apoptosis rate and cell number between the normoxia and normoxia + PFTBA groups ($P > 0.05$, Fig. 3F). After hypoxic treatment of 48 h, the apoptosis rate in the hypoxia group was significantly increased to 23.27 ± 2.53%, which is in contrast to 5.76 ± 0.26% in the normoxia group, indicating the detrimental effect of hypoxia on AFSCs. While in the hypoxia + PFTBA group, the apoptosis rate was significantly decreased, with an apoptosis rate of 8.2 ± 1.4% (Fig. 3F), indicating that the oxygen released from the PFTBA fibers was capable of protecting AFSCs from hypoxia-induced apoptosis. In the meantime, surviving cells were counted at 48 h, 96 h, and 144 h *via* phalloidin and DAPI staining, respectively (Fig. 3E). Under normoxia, the number of cells was not significantly altered by PFTBA fibers (Fig. 3G). However, under hypoxia, the number of cells was significantly increased by PFTBA fibers, further confirming the protective effect of oxygen from PFTBA fibers on AFSCs under hypoxic condition (Fig. 3G).

CCK-8 was then used to evaluate cell proliferation. It was revealed that the cell proliferation in hypoxia + PFTBA group was significantly higher than that in the hypoxia group after 48 h, 96 h, and 144 h of hypoxic treatment (Fig. 3H), indicating that PFTBA fibers promoted AFSCs proliferation under hypoxia. SEM was then used to evaluate the morphology of AFSCs on the core-shell fiber membrane containing PFTBA (Fig. 3I). After 144 h of hypoxia, the AFSCs in the hypoxic group were apoptotic and shrunken, showing a state of disintegration. In contrast, cells in the hypoxia + PFTBA group exhibited a steady-state morphology, similar to the normoxia group. Those results indicated that the core-shell oxygen supply fibers were capable of promoting the proliferation of AFSCs under hypoxia.

3.4. Differentially expressed mRNAs in AFSCs with/without PFTBA under hypoxia

Transcriptome was performed to further elucidate the molecular events underlying the protective effect of the PFTBA-released oxygen on AFSCs under hypoxic conditions. As shown in the volcano plot, 58 up-regulated and 175 down-regulated DEGs were detected between the hypoxia and hypoxia + PFTBA groups (Fig. 4A). To better understand the potential functions of DEGs between these two treatment groups, GO enrichment was performed (Fig. 4B and C). Among the down-regulated DEGs, we observed participation in “positive regulation of cell proliferation” (e.g., Wnt5a, Hmox1, Agtr2), “response to hypoxia” (e.g., Aqp3, Nr4a2, Hmox1), and “stem cell proliferation” (e.g., Cxcl1, Scrg1, Wnt5a) in the PFTBA-treated AFSCs, which was consistent with the findings in the previous section. In contrast, the “positive regulation of response to stimulus” (e.g., Rspo3, Cdh13, Adamsts3), “regulation of cellular component organization” (e.g., Nanos1, Nod2, Plxna4), and “cell migration” (e.g., Nanos1, Hoxb9, Lrrc15) related genes were up-regulated in the PFTBA-treated AFSCs, which were also verified by qPCR results (Fig. 4D and Fig. S3). Moreover, DEGs in the PFTBA-treated AFSCs were also enriched in functional annotations related to cell adhesion and growth, as well as the TGF-beta and PI3K-Akt signaling pathways in the KEGG pathway analysis (Fig. 4E). In addition, gene set enrichment analysis (GSEA) results further confirmed the enhanced proliferation-promoting and cell cycle function enrichment (Fig. 4F) in the PFTBA-treated cells.

Synthesis of cellular components and cell migration function, which were enriched in the DEGs in the present study, play a vital role in the regeneration and repair of various tissue injuries and stem cell therapies [40,41]. Therefore, we subsequently analyzed the cellular components and migratory function of the AFSCs under hypoxia culture with or without PFTBA fibers. We demonstrated that the collagen I and III gene expressions were significantly up-regulated in the PFTBA group (Fig. 5A–E). Moreover, the PFTBA core shell fibers significantly enhanced the migratory ability of AFSCs under hypoxia (Fig. 5F and G). These findings suggested that oxygen from PFTBA fibers was capable of promoting expression of cellular components and enhancing migration of AFSCs under hypoxia condition, thus highlighting the therapeutic potential of the oxygen-releasing materials in promoting AF repair by enhancing the AFSC function.

3.5. Radiographic improvements of IVD degeneration using PFTBA fibers in vivo

In order to evaluate the repair effect of PFTBA fibers *in vivo*, a rat tail

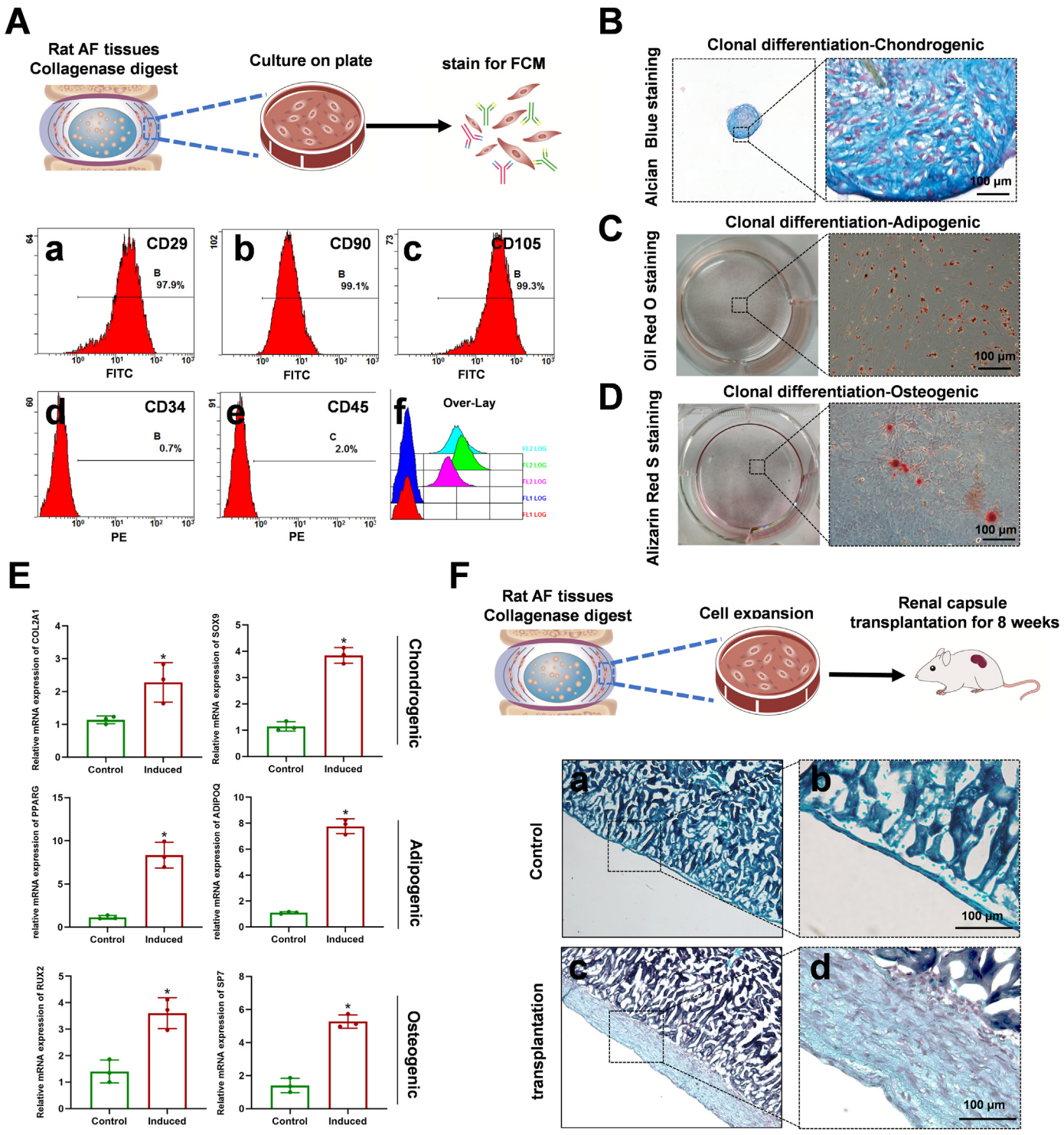

Fig. 2. Functional identification of AFSCs *in vitro* and *in vivo*. (A) The work flow for characterization of AFSCs *in vitro* (top). FCM analysis showed that the primary AFSCs expressed highly abundant stem cell markers CD29, CD90, and CD105, but not hematopoietic markers CD34 and CD45. (B–D) Representative Alcian Blue, Oil Red O, and Alizarin Red staining after chondrogenic, adipogenic, and osteogenic differentiation of AFSCs. (E) qPCR analysis of chondrogenic, adipogenic, and osteogenic marker genes in AFSCs before and after *in vitro* trilineage differentiation (n = 3). (F) The work flow for characterization of AFSCs *in vivo* (top). Eight weeks post renal capsule transplantation of AFSCs in immunodeficient mice, SOFG staining revealed that AFSCs displayed fibrotic differentiation ability. $^{*}p < 0.05$ vs. Control group.

disc AF defect model was constructed and repaired by PFTBA fibers. All animals were subjected to X-ray and MRI scans at 2, 4 and 8 weeks post operation/treatment, as well as micro-CT scans at 8 weeks post treatment (Fig. 6A and B). As shown in Fig. 6Ca-d, loss of IVD height was observed in Defect and Fiber groups under X-ray scan, while the disc height index in the PFTBA group was significantly higher than the remaining groups (Fig. 6D). Based on the MRI scanning, the maintenance of the native NP hydration and morphology was observed in the PFTBA fiber group. In contrast, an intradiscal nuclear signal loss was present in the Defect and the Fiber groups after 8 weeks (Fig. 6Ce-h). In addition, the degeneration

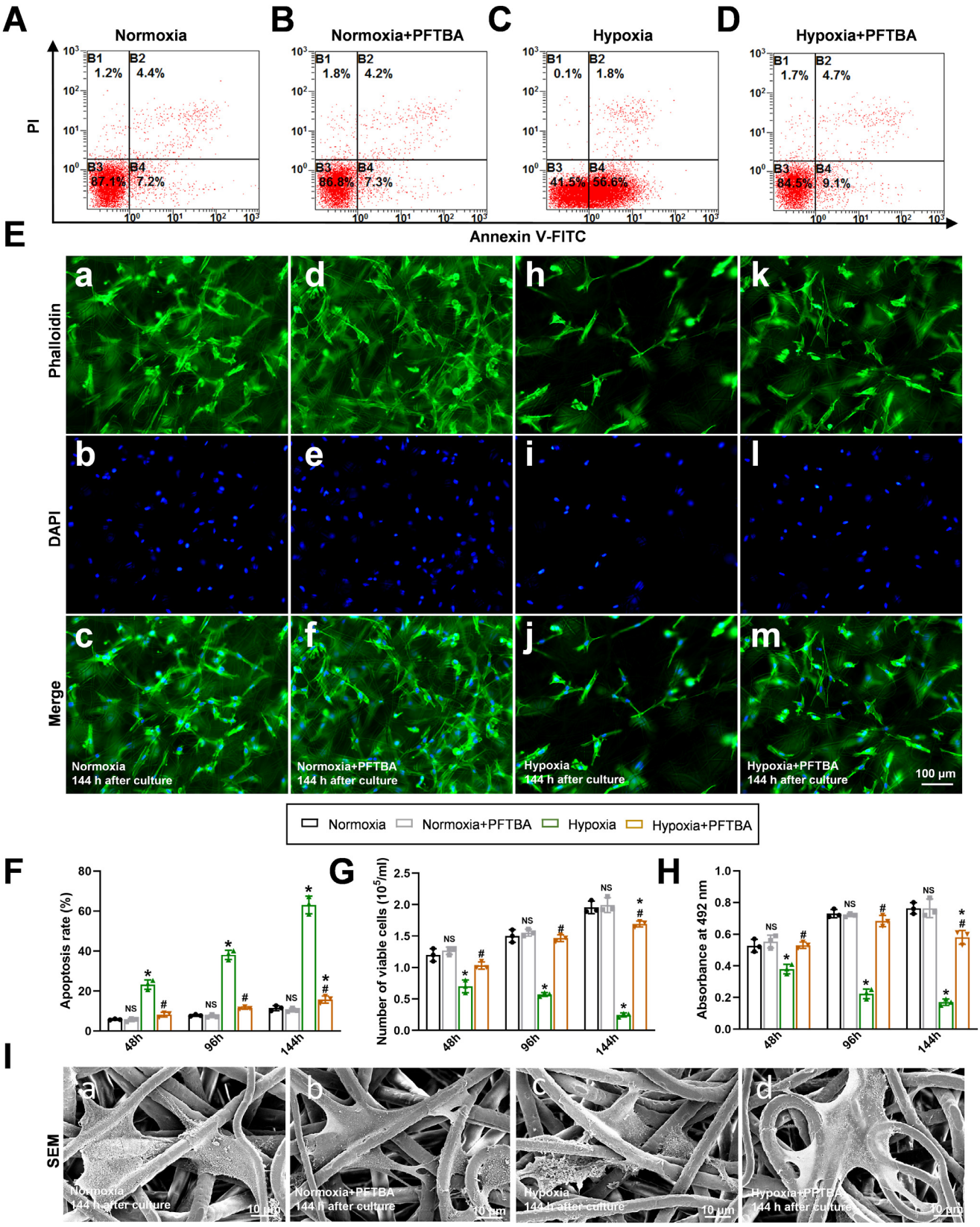

Fig. 3. Effect of PFTBA fibers on regulating AFSCs viability and proliferation under hypoxia *in vitro*. (A–D) FCM detection of cell apoptosis, (E) Phalloidin and DAPI staining of AFSCs on fibers. (F) Apoptosis assay, (G) cell number count and (H) CCK-8 values in each group were obtained by averaging the results of 3 samples per group. (I) SEM showing cell microscopic morphology. All data are presented as mean ± SD. $^{*}p < 0.05$ vs. Normoxia group. $^{\#}p < 0.05$ vs. Hypoxia group. NS: no significant difference vs. Normoxia group.

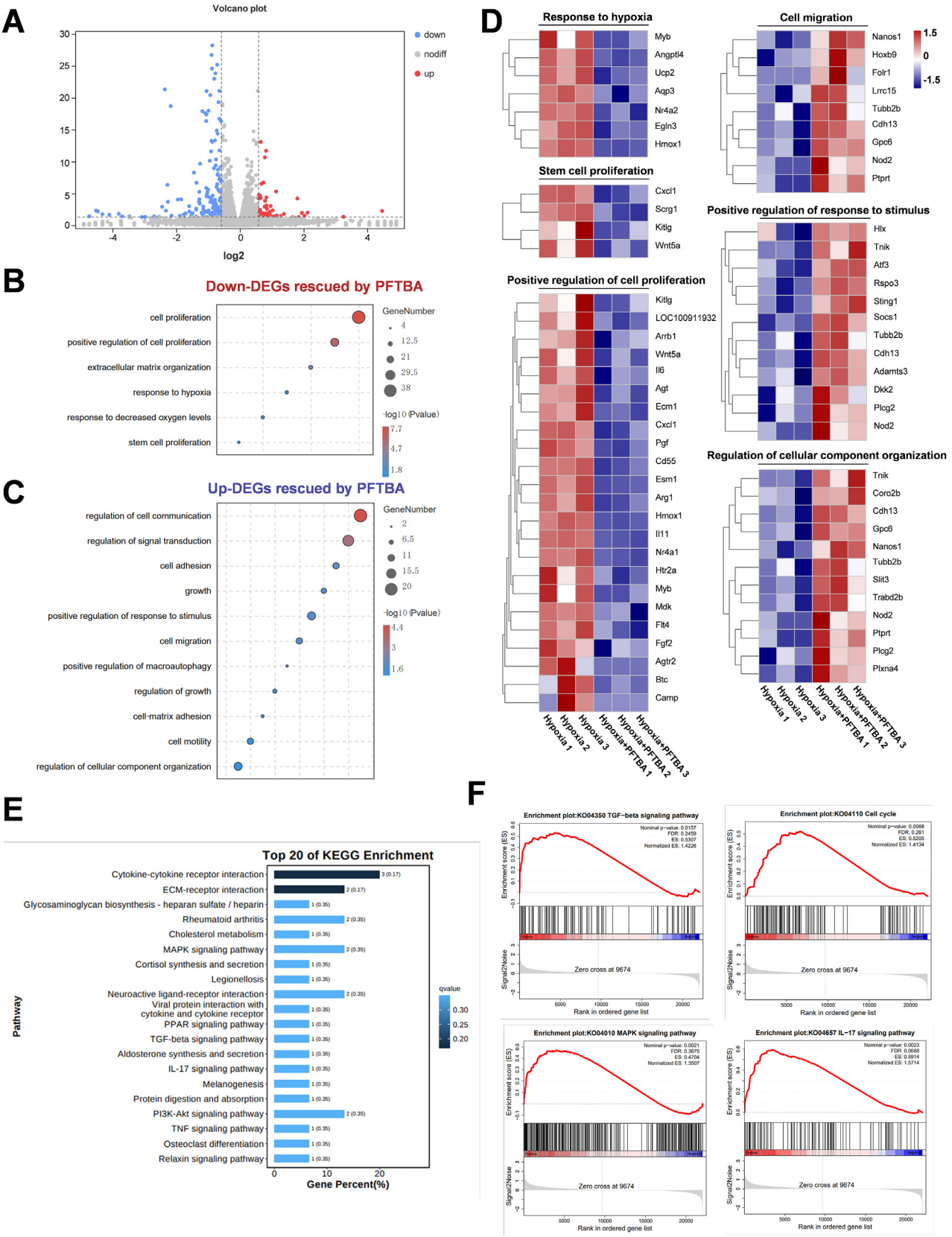

Fig. 4. Transcriptome profiles in AFSCs with/without PFTBA under hypoxia. (A) DEG volcano map comparing the Hypoxia vs. Hypoxia + PFTBA groups. Red dots represent 58 markedly elevated DEGs; blue dots represent 175 markedly reduced DEGs; and gray dots represent no change. (B) Dots plots representing significantly GO enriched terms of down-DEGs in two groups. (C) Dots plots representing significantly GO enriched terms of up-DEGs in two groups. (D) Heatmap showing the relative expression levels of DEGs associated with indicated terms in two groups. (E) KEGG enrichment showing top 20 pathways. (F) gene set enrichment analysis results in the PFTBA-treated AFSCs.

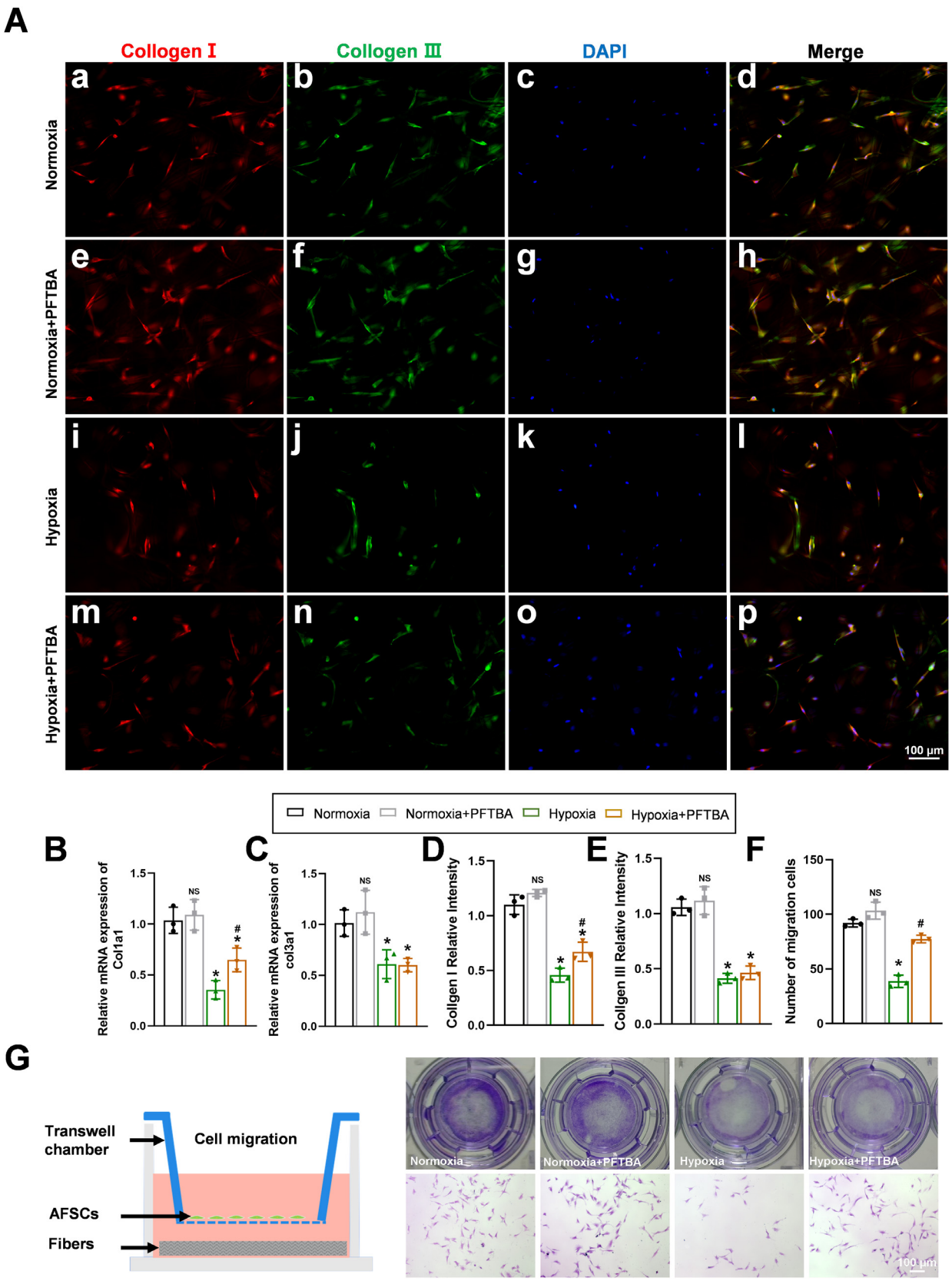

Fig. 5. Effect of PFTBA fibers on expression of cellular components and migration ability of AFSCs *in vitro*. (A) Representative immunofluorescence images of collagen I and collagen III in AFSCs. (B–E) The qRT-PCR analysis of col1a1 and col3a1 transcripts (n = 3), semi-quantitative analysis of collagen I and collagen III fluorescence intensity in AFSCs (n = 3). (F and G) The representative images of migrating AFSCs and number count of migrating AFSCs in each group. $^{*}p < 0.05$ vs. Normoxia group. $^{\#}p < 0.05$ vs. Hypoxia group. NS: no significant difference vs. Normoxia group.

Pfirrmann score was significantly improved in the PFTBA group compared to the Defect and Fiber groups at each time point (Fig. 6E), confirming the long-term therapeutic effect of the PFTBA fiber on IVD degeneration. By micro-CT, the maintenance of intervertebral space height and reduction of perivertebral osteophyte formation in IVD were observed in the PFTBA fiber group (Fig. 6Ci-p). Moreover, the PFTBA fiber group exhibited significantly decreased endplate bone volume (BV/TV), compared to the Defect and Fiber groups, indicating less degeneration of endplate in the IVD of PFTBA fibers group (Fig. 6F). Additionally, no obvious difference in bone mineral density (BMD) was observed between groups (Fig. 6G). Collectively, the radiographic findings indicated that the PFTBA fibers with PFTBA was capable of reducing post-injury IVD degeneration in rats *in vivo*.

3.6. Histological improvement of AF defect by PFTBA fibers in vivo

The morphological alterations at the site of AF defect were evaluated using SOFG and Sirius red staining (Fig. 7A). In this study, the IVD exhibited obvious defect space and loss of NP tissue in the Defect group, which might result in the disruption of collagen orientation and the cleft extending into the inner AF. In the Fiber group, although relatively ordered AF structure and collagen orientation were observed, absence of NP tissue was still evident. In the PFTBA fiber group, the AF structure exhibited enhanced orderly arrangement, and obvious collagen repair in the outer AF layer was present under polarized light and more NP cells were retained (Fig. 7Ae-h). These histological results demonstrated the beneficial effect of PFTBA fibers on the repair of the AF defect. Furthermore, the quantitative analysis showed a markedly higher number of NP cell and larger NP area in the PFTBA group versus the Defect and Fiber groups (Fig. 7B and C). In addition, the histological score and the area of type I and type III collagen was highest in the Defect group, followed by the Fiber group, and least in the PFTBA and control groups (Fig. 7D and E), indicating better repair efficiency of PFTBA fibers in histological assessment.

We also assessed the biocompatibility, chronic inflammation and immune responses to the implanted material at the defect site using SEM and H&E staining (Fig. 7F and G). No immune infiltration was observed in the NPs, AFs, or endplates adjacent to the implanted material in the PFTBA fiber groups Taken together, these findings confirmed the beneficial effect of oxygen released from PFTBA fibers on the repair of AF defect.

3.7. In vivo gene expression profile by PFTBA fibers

To further reveal the underlying molecular events induced by PFTBA fiber treatment *in vivo*, we compared the transcriptome between the Fiber and PFTBA fiber groups. As illustrated in the volcano plot, there were 71 DEGs between the Fiber and PFTBA fiber groups (Fig. 8A). To better understand the potential functions of DEGs between these two treatment groups, GO enrichment was performed (Fig. 8B). We observed that DEGs were involved in “oxygen binding” and “oxygen transport”, further confirming the participation of oxygen in the AF defect repair. Interestingly, “angiogenesis” was also enriched in the DEGs. Next, in order to investigate the potential involvement of angiogenesis we characterized the CD34-positive cell at the defect site *via* immunofluorescence staining. Compared to the Fiber group, more blood vessel formation was observed in the PFTBA fiber group, and the CD34-positive staining area was significantly higher in the PFTBA fiber group (Fig. 8C and D), indicating that the PFTBA fiber contributes to the formation of blood vessels at the defect site. Next, we took a closer look at the cell types involved at the defect site. FSP1(fibroblast specific protein 1) and COL1 were used to label the fibroblast and AF cells at the site of AF defect, respectively (Fig. 8E and G). It was found that the FSP1 positive cells were present in the Defect, Fiber and PFTBA fiber groups, showing the involvement of fibroblast cells in AF defect repair. In addition, the number of the FSP1 positive cells were the highest in the Defect group, followed by the Fiber group, indicating that there was more fibrous scar formation at the AF defect sites in these two groups. However, fewer FSP-1 positive cells were present in the PFTBA fiber group, suggesting that less fibrous scar was formed in the PFTBA fiber group. To further observe AF regeneration at the injured site, immunofluorescence staining of COL1, a major matrix component in the outer AF, was employed to denote endogenous regeneration as described in previous studies [39,42]. COL1 was highly expressed in the sham group, but was significantly reduced in the defect and fiber groups (Fig. 8F and H). This phenomenon was significantly restored in the PFTBA group, suggesting that there was more regeneration was present in the PFTBA fiber group than the defect and fiber groups. Collectively, these findings support that the PFTBA fibers are capable of promoting AF repair and regeneration.

4. Discussion

Clinically, discectomy can effectively relieve IVD herniation symptoms, however, it typically leaves a large defect in the AF tissue [43]. Thus far, due to lack of nutrition supply at the surgery site (such as lack of oxygen supply), the AF defect site repair has always been challenging [16,17]. In this study, we established a PFTBA based oxygen supply fibers *via* coaxial electrospinning. The PFTBA-encapsulated fibers released oxygen for about 144 h, which enhanced the survival rate and migration capacity of AFSCs under hypoxic conditions *in vitro*. Furthermore, our *in vivo* studies revealed that the PFTBA-based oxygen system was capable of promoting AF regeneration. These findings suggested that the PFTBA-based oxygen carriers markedly enhanced cell viability by increasing oxygen release, thus, raising a possibility of using PFTBA-based oxygen-releasing systems to protect AFSCs, thus promoting AF tissue regeneration after discectomy.

Oxygen is a metabolite necessary for the survival and function of aerobic organisms [44,45]. In the early stage of tissue injury, hypoxia is unfavorable for tissue regeneration, especially in a poorly vascularized microenvironment, which generally induces oxidative stress, apoptosis and necrosis, thereby accelerating cell death [46]. In recent years, the issue of local hypoxia in skin healing, bone regeneration and nerve repair has gained increasing attention, and studies have clarified the beneficial effects of local oxygen supply on tissue regeneration and repair [47–50]. However, the effect of local oxygen supply on tissue regeneration during the AF repair is still unclear.

At present, a variety of oxygen-releasing materials have been developed to counteract local hypoxia by directly supplying oxygen to the implanted structure [51–53]. Meanwhile, a variety of materials can be used as oxygen releasing sources, among which, the commonly used materials are calcium peroxide, magnesium peroxide, and PFTBA [53–55]. Compared to peroxides, PFTBA has less biocompatibility concern, and can directly provide oxygen to cells without chemical reaction [33]. Nevertheless, a common problem in oxygen delivery systems is the sudden release of oxygen [56]. The rapid generation of oxygen results in the release of hydroxyl radicals, which can lead to the formation of peroxide conditions and cell damage [57]. One strategy to prevent this phenomenon is to encapsulate the oxygen sources into polymeric materials by means of emulsion, microfluidic fabrication, solvent casting, or electrospinning [53,58]. In this study, we employed coaxial electrospinning technology to form a core-shell scaffold that served as a carrier of oxygen. Using electrospinning, a coaxial structure was formed by inserting a smaller capillary into a larger capillary in a concentric fit [59,60]. Compared to the solid fiber structure, core-shell fiber has advantages in tuning release kinetics and initial burst release [59]. More importantly, when the additives are loaded on the core structure, the shell layer can not only act as an outer protective layer but also tune the release of additives from fibers [60]. By adjusting the parameters (the ratio of chitosan to PCL and the concentration of chitosan), the structure of the coaxial electrospinning material showed great variations, and stable core shell fibers were established by 5 sets of parameters *via* coaxial electrospinning in our study. Further analysis revealed that one set of

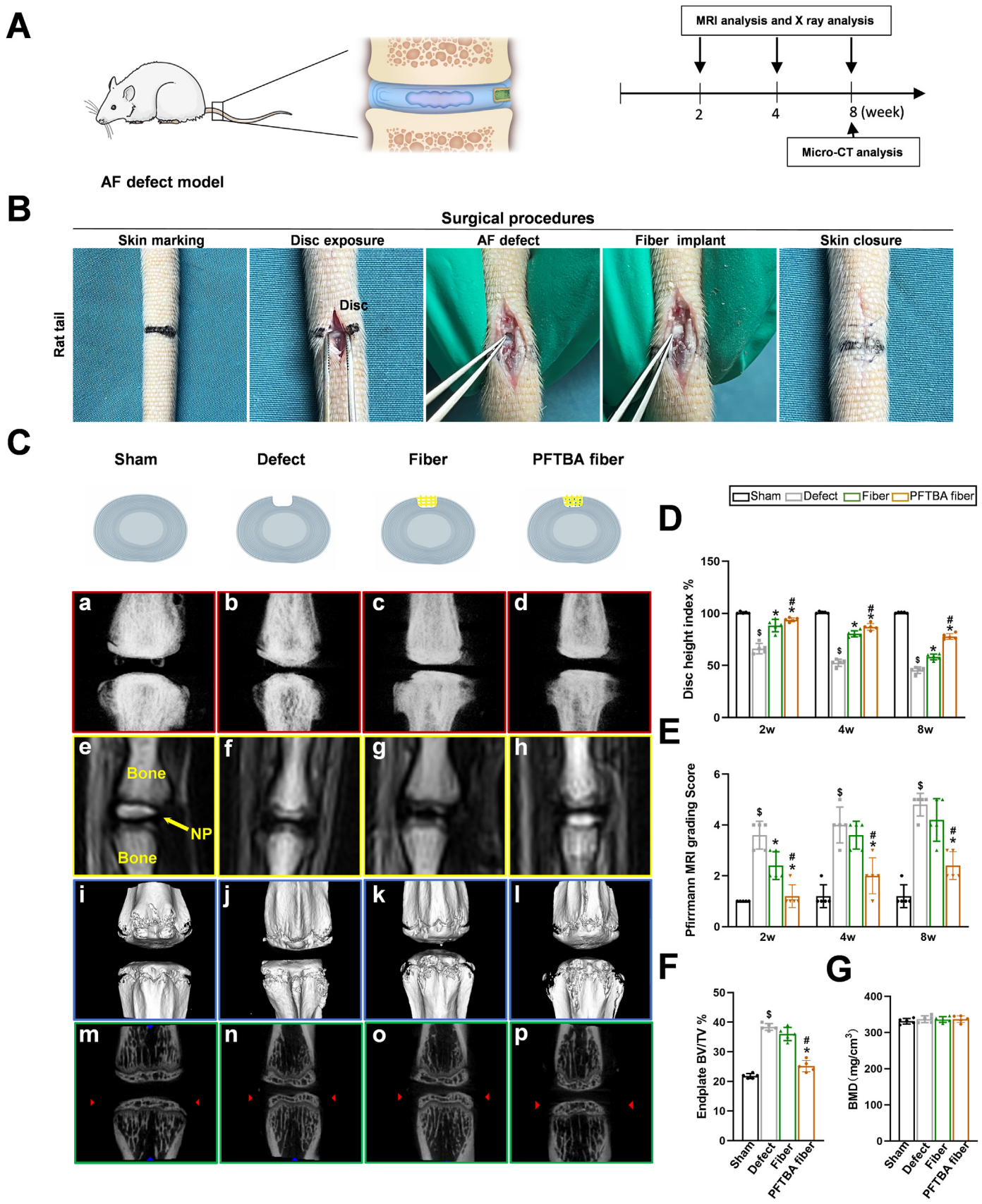

Fig. 6. Radiographic improvements of IVD degeneration by PFTBA fibers *in vivo*. (A) A schematic illustration of the experimental procedures in rats. (B) Representative images of surgical procedures. (C) Representative imaging results. The scheme (top) and imaging characteristics of each group after 8 weeks treatment, including X-ray (a–d), MRI (e–h) and Micro-CT (i–p). (D–G) Quantitative analysis of disc height index (%DHI), Pfirrmann grading score, endplate bone volumes (BV/TV) and bone mineral density (BMD) in each group (n = 5). $^{\$}p < 0.05$ vs. Control group. $^{*}p < 0.05$ vs. Defect group. $^{\#}p < 0.05$ vs. Fiber group.

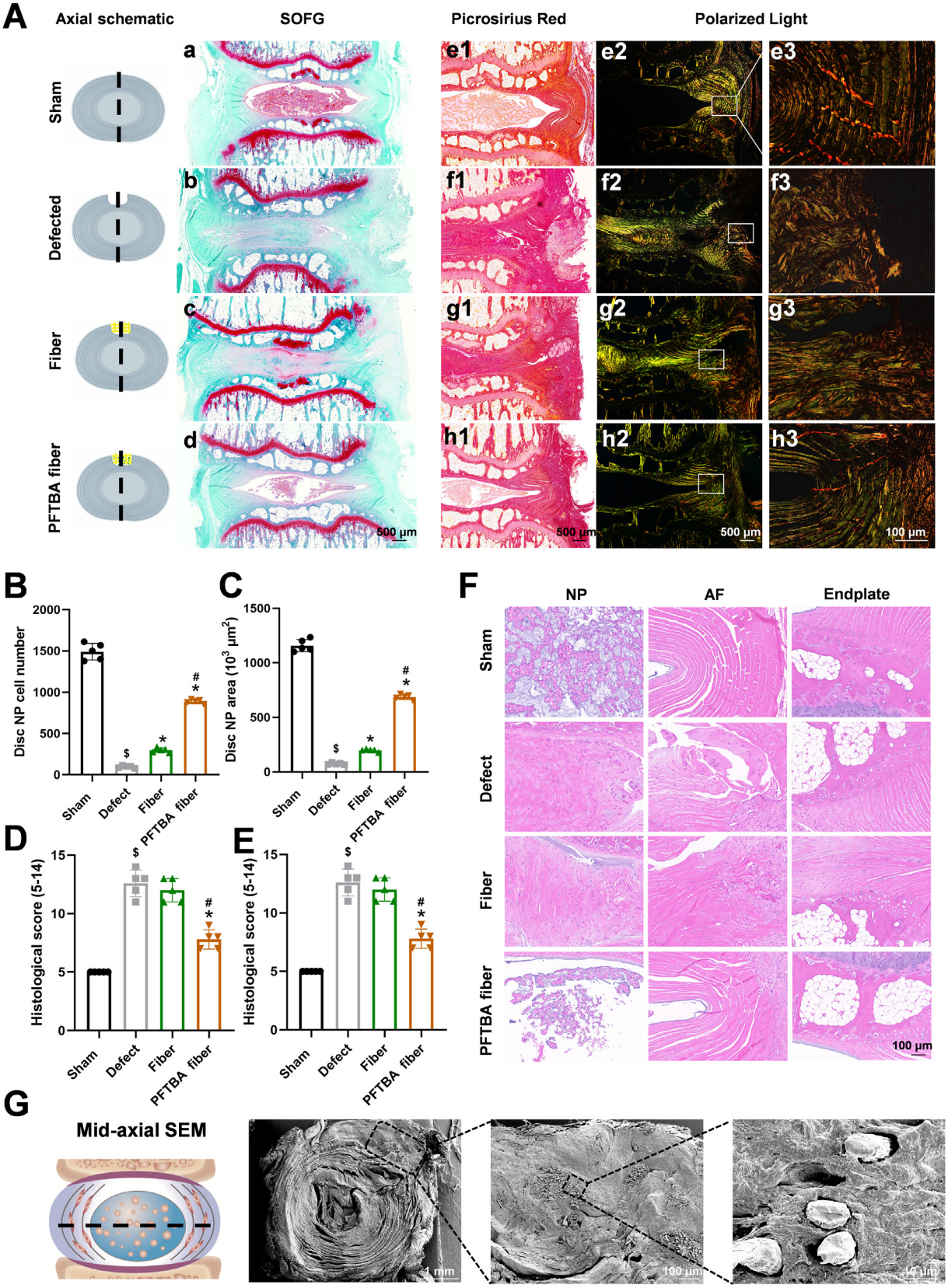

Fig. 7. Effect of PFTBA fibers on histological recovery during AF repair at 8 weeks after treatment. (A) The schematic diagram of the tissue section site (left) and representative images of IVD tissue SOFG staining (a–d), and Sirius Red staining (e–h). (B–E) Quantitative analysis of disc NP cell number, disc NP area, histological score and percentage of type I and type III collagen area in each group (n = 5). (F) Representative images of IVD tissue H&E staining. (G) Representative mid-axial morphology in AF defect site under SEM. $^{\$}p < 0.05$ vs. Control group. $^{*}p < 0.05$ vs. Defect group. $^{\#}p < 0.05$ vs. Fiber group.

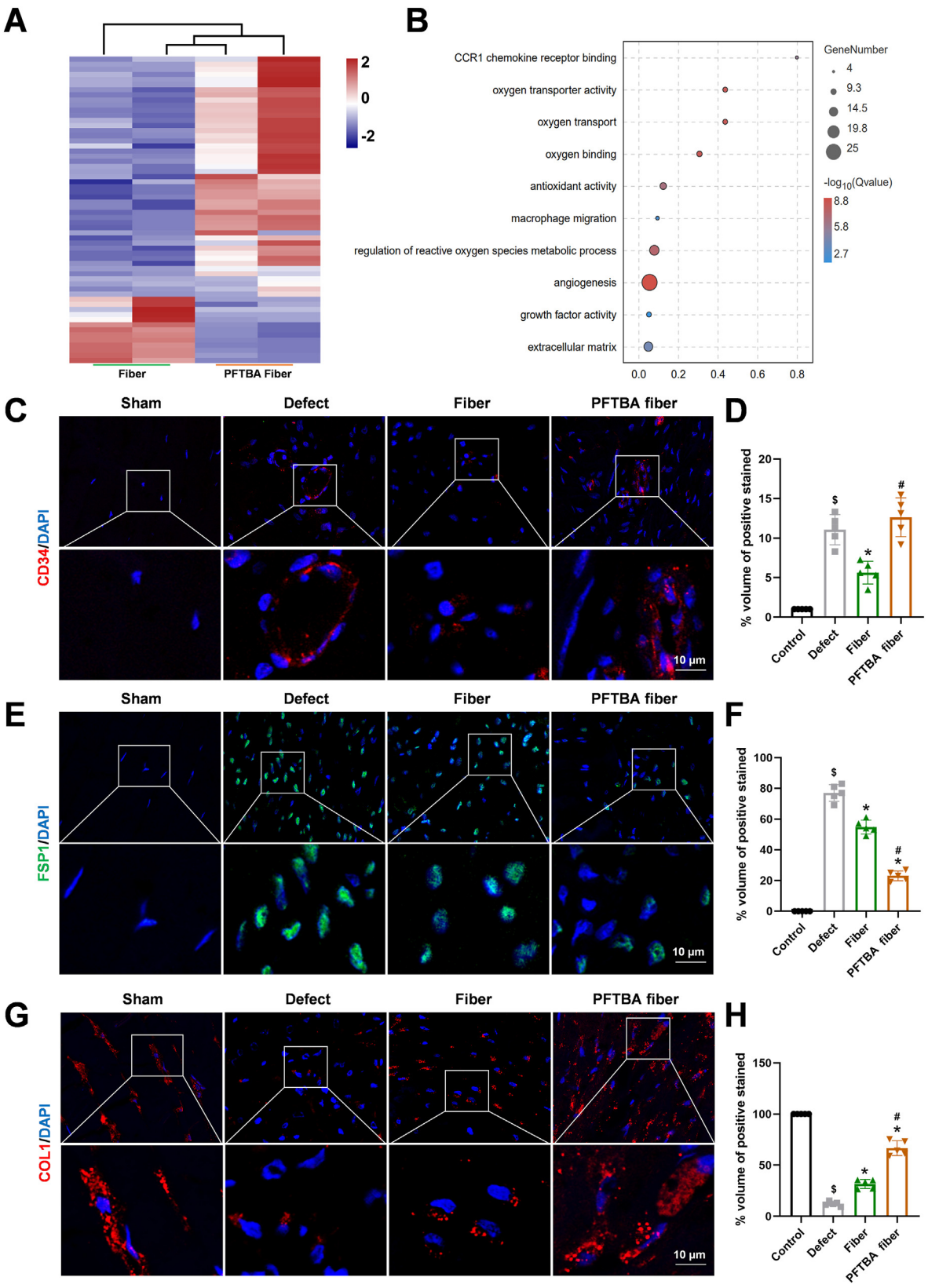

Fig. 8. The underlying molecular events induced by PFTBA fiber treatment *in vivo*. (A) DEG heatmap between the Fiber and PFTBA fiber groups. (B) GO terms. (C–H) Representative images of immunofluorescence and semi-quantitative analysis of CD34, FSP1 and COL1 fluorescence intensity in IVD tissues, imaged by fluorescence microscopy (n = 5). $^{\$}p < 0.05$ vs. Control group. $^{*}p < 0.05$ vs. Defect group. $^{\#}p < 0.05$ vs. Fiber group.

parameters (10% chitosan, chitosan: PCL, 1:6) prolonged the time course of oxygen release, up to 144 h, and the oxygen level was maintained at an appropriate level in the surrounding medium. The slow release of oxygen might be attributable to its uniform ultrastructure and high specific surface area composition of spinning.

Successful AF repair and regeneration requires restoration of the biomechanical and structural properties, and the biological behavior of resident cells within AF [61,62]. AFSCs are essential candidate cells in the process of AF regeneration and repair [13,63]. AFSCs can migrate from their niche to the defect site to maintain AF cell populations [39]. In this study, we demonstrated that the AFSCs possess colony formation ability, express typical MSC markers, and possess the ability of tri-lineage differentiation potential, which were different from AF cells. Previous studies revealed that the endogenous stem cells can be recruited using chemoattractants (CXCR4, CCL5, and SDF-1) to enhance the therapeutic potential of biomaterials in repairing AF defects [64–66]. However, the niche cells and recruited stem cells often encounter an unfavorable local microenvironment (such as, compression and hypoxia), which leads to excessive cellular death [9,13,16]. From the *in vitro* oxygen releasing kinetics, we can see that the oxygen concentration in the hypoxia + PFTBA groups was higher than hypoxia alone group, however, it did not reach the oxygen level in the normoxia group. Moreover, the mRNA levels of representative genes including Hoxb9, Nod2, Cdh13, Adamts3 and Plxna4 in the hypoxia + PFTBA were comparable between normoxia and hypoxia groups, indicating an intermediate state of cells in hypoxia + PFTBA group. These *in vitro* results indicated that oxygen release from PFTBA core-shell fibers can partially alleviate hypoxia-induced dilemma. In future studies, the transcriptional difference between the hypoxia + PFTBA and normixia groups are of value in further explaining the treatment effect of PFTBA, and worthy of investigations.

In the *in vivo* repair studies, the morphological alterations in the PFTBA group also presented an enhanced repair in the defect sites. It is generally recognized that normal IVD is composed of ECM-rich NP tissue and structurally intact AF. The NP tissue is squeezed and quickly pressured when the IVD experiences stress, thus, causing it to stretch outward into the AF. By preventing NP protrusion and resisting stretching and twisting, AF contributes to the load-bearing process, which results in the mixture of compressive, tensile, and shear forces [67]. Once AF fails, the soft central NP tissue is extruded from the lesion, which compromises the integrity of the IVD complex, thus resulting in impaired mechanical function, inflammation, and aggravated tissue degeneration [68]. In this study, we observed that the number and area of NP cells in the PFTBA fiber group were more preserved, which might be attributed to the augmented AF tissue regeneration at the defect site, which, in turn, inhibited the protrusion of NP tissue and additional degeneration of the IVD. Taken together, these findings suggested that the PFTBA-based oxygen delivery system is capable of promoting AF regeneration by enhancing oxygen delivery, thereby slowing down IVD degeneration.

We next examined the molecular events elicited by PFTBA fiber during *in vivo* AF repair and regeneration. It was revealed that DEGs were enriched in oxygen-related functions, such as “oxygen binding” and “oxygen transport”. In addition, we also observed differences in “angiogenesis” at the transcriptome level, suggesting that local oxygen release alleviated the severity of hypoxia within implants, tune hypoxia to a less serious level, which might be more favorable for vascularization. Previous studies emphasized the importance of oxygen supply in implants during the tight coupling of angiogenesis and tissue regeneration, such as bone and neural tissue [69–71]. In this study, the blood vessel formation in the PFTBA fiber group was significantly increased, compared to the Fiber group, which confirmed that the PFTBA fiber holds the potential of tuning the oxygen tension for the formation of blood vessels, paving a new avenue for achieving the long-term maintenance of nutrient supply at the defect site.

Although the results are exciting, the current study had several limitations. Due to the difficulties of measuring the exact tissue oxygen level, it is still a challenge to identify the oxygen release kinetics of the PFTBA implants *in vivo* and future studies that monitor the oxygen level within a specific tissue *in vivo* would add significant value for oxygen related studies. In addition, concerning the practical anatomical location, low cost and high reproducibility of the rat tail disc model, rats were employed with the assistance of microscopy and microscopic instruments in this study. However, the advantages of manipulation in large animals' disc are undeniably superior to those in small animals. Future investigations are warranted in larger animal models, and the results need to be contextualized in order to understand how treatments may be used in humans.

5. Conclusion

A PFTBA core-shell oxygen supply scaffold was fabricated using coaxial electrospinning. The oxygen released from the PFTBA fibers protected AFSCs from the hypoxia-induced cell death, and promoted cell migration and ECM production. In addition, the oxygen supply fibers successfully prevented degeneration after discectomy in a rat model, thus, highlighting the potential of the oxygen supply system during AF repair.

Credit authors statement

Yi Zheng: Methodology, Conceptualization, Formal analysis, Data curation, Writing-original draft. **Borui Xue**: Validation, Investigation, Writing- original draft. **Bin Wei**: Formal analysis, Investigation, Methodology. **Bin Xia**: Resources, Conceptualization. **Shengyou Li**: Data curation, Visualization. **Xue Gao**: Software, Validation. **Yiming Hao**: Resources, Visualization. **Yitao Wei**: Resources. **Lingli Guo**: Validation. **Haining Wu**: Methodology, Investigation. **Yujie Yang**: Methodology, Software. **Xueli Gao**: Data curation. **Beibei Yu**: Software. **Yongfeng Zhang**: Visualization. **Shijie Yang**: Software. **Zhuojing Luo**: Project administration, Supervision, Funding acquisition, Writing-review & editing. **Teng Ma**: Methodology, Conceptualization, Funding acquisition, Writing-review & editing. **Jinghui Huang**: Supervision, Conceptualization, Project administration, Funding acquisition, Writing-review & editing.

Declaration of competing interest

The authors declare that they have no known competing financial interests or personal relationships that could have appeared to influence the work reported in this paper.

Data availability

Data will be made available on request.

Acknowledgements

This work was supported by grants from the National Natural Science Foundation of China (82122043 and 81972052) and China Postdoctoral Science Foundation (2021M693946, 2020T130788 and 2019M653967).

Appendix A. Supplementary data

Supplementary data to this article can be found online at https://doi.org/10.1016/j.mtbio.2022.100535.

References

[1] J. Hartvigsen, M.J. Hancock, A. Kongsted, Q. Louw, M.L. Ferreira, S. Genevay, D. Hoy, J. Karppinen, G. Pransky, J. Sieper, R.J. Smeets, M. Underwood, What low back pain is and why we need to pay attention, Lancet 391 (10137) (2018) 2356–2367.

[2] S. Kirnaz, C. Capadona, T. Wong, J.L. Goldberg, B. Medary, F. Sommer, L.B. McGrath Jr., R. Härtl, Fundamentals of intervertebral disc degeneration, World Neurosurg. 157 (2022) 264–273.

[3] J.M. Stevans, A. Delitto, S.S. Khoja, C.G. Patterson, C.N. Smith, M.J. Schneider, J.K. Freburger, C.M. Greco, J.A. Freel, G.A. Sowa, A.D. Wasan, G.P. Brennan, S.J. Hunter, K.I. Minick, S.T. Wegener, P.L. Ephraim, M. Friedman, J.M. Beneciuk, S.Z. George, R.B. Saper, Risk factors associated with transition from acute to chronic low back pain in US patients seeking primary care, JAMA Netw. Open 4 (2) (2021), e2037371.

[4] P. Yu, F. Mao, J. Chen, X. Ma, Y. Dai, G. Liu, F. Dai, J. Liu, Characteristics and mechanisms of resorption in lumbar disc herniation, Arthritis Res. Ther. 24 (1) (2022) 205.

[5] P.S. Gadjradj, B.S. Harhangi, J. Amelink, J. van Susante, S. Kamper, M. van Tulder, W.C. Peul, C. Vleggeert-Lankamp, S.M. Rubinstein, Percutaneous transforaminal endoscopic discectomy versus open microdiscectomy for lumbar disc herniation: a systematic review and meta-analysis, Spine (Phila Pa 46 (8) (1976) 538–549, 2021.

[6] D.R. Esfahani, H. Shah, G.D. Arnone, J.K. Scheer, A.I. Mehta, Lumbar discectomy outcomes by specialty: a propensity-matched analysis of 7464 patients from the ACS-NSQIP database, World Neurosurg. 118 (2018) e865–e870.

[7] S.S. Rudisill, A.L. Hornung, J.N. Barajas, J.J. Bridge, G.M. Mallow, W. Lopez, A.J. Sayari, P.K. Louie, G.K. Harada, Y. Tao, H.J. Wilke, M.W. Colman, F.M. Phillips, H.S. An, D. Samartzis, Artificial intelligence in predicting early-onset adjacent segment degeneration following anterior cervical discectomy and fusion, Eur. Spine J. 31 (8) (2022) 2104–2114.

[8] P. Heindel, A. Tuchman, P.C. Hsieh, M.H. Pham, A. D'Oro, N.N. Patel, A.M. Jakoi, R. Hah, J.C. Liu, Z. Buser, J.C. Wang, Reoperation rates after single-level lumbar discectomy, Spine (Phila Pa 42 (8) (1976) E496–e501, 2017.

[9] C.C. Guterl, E.Y. See, S.B. Blanquer, A. Pandit, S.J. Ferguson, L.M. Benneker, D.W. Grijpma, D. Sakai, D. Eglin, M. Alini, J.C. Iatridis, S. Grad, Challenges and strategies in the repair of ruptured annulus fibrosus, Eur. Cell. Mater. 25 (2013) 1–21.

[10] M. Gugliotta, B.R. da Costa, E. Dabis, R. Theiler, P. Jüni, S. Reichenbach, H. Landolt, P. Hasler, Surgical versus conservative treatment for lumbar disc herniation: a prospective cohort study, BMJ Open 6 (12) (2016), e012938.

[11] K.R. Nakazawa, B.A. Walter, D.M. Laudier, D. Krishnamoorthy, G.E. Mosley, K.L. Spiller, J.C. Iatridis, Accumulation and localization of macrophage phenotypes with human intervertebral disc degeneration, Spine J. 18 (2) (2018) 343–356.

[12] J.P. Urban, S. Smith, J.C. Fairbank, Nutrition of the intervertebral disc, Spine (Phila Pa 29 (23) (1976) 2700–2709, 2004.

[13] A.P. Peredo, S.E. Gullbrand, R.L. Mauck, H.E. Smith, A challenging playing field: identifying the endogenous impediments to annulus fibrosus repair, JOR Spine 4 (1) (2021) e1133.

[14] L.J. Smith, D.M. Elliott, Formation of lamellar cross bridges in the annulus fibrosus of the intervertebral disc is a consequence of vascular regression, Matrix Biol. 30 (4) (2011) 267–274.

[15] F. Mwale, I. Ciobanu, D. Giannitsios, P. Roughley, T. Steffen, J. Antoniou, Effect of oxygen levels on proteoglycan synthesis by intervertebral disc cells, Spine (Phila Pa 36 (2) (1976) E131–E138, 2011.

[16] Y.C. Huang, V.Y. Leung, W.W. Lu, K.D. Luk, The effects of microenvironment in mesenchymal stem cell-based regeneration of intervertebral disc, Spine J. 13 (3) (2013) 352–362.

[17] K. Ma, S. Chen, Z. Li, X. Deng, D. Huang, L. Xiong, Z. Shao, Mechanisms of endogenous repair failure during intervertebral disc degeneration, Osteoarthritis Cartilage 27 (1) (2019) 41–48.

[18] G. Chu, W. Zhang, F. Han, K. Li, C. Liu, Q. Wei, H. Wang, Y. Liu, F. Han, B. Li, The role of microenvironment in stem cell-based regeneration of intervertebral disc, Front. Bioeng. Biotechnol. 10 (2022), 968862.

[19] Q. Wei, D. Liu, G. Chu, Q. Yu, Z. Liu, J. Li, Q. Meng, W. Wang, F. Han, B. Li, TGF-β1-supplemented decellularized annulus fibrosus matrix hydrogels promote annulus fibrosus repair, Bioact. Mater. 19 (2023) 581–593.

[20] C. Yu, D. Li, C. Wang, K. Xia, J. Wang, X. Zhou, L. Ying, J. Shu, X. Huang, H. Xu, B. Han, Q. Chen, F. Li, J. Tang, C. Liang, N. Slater, Injectable kartogenin and apocynin loaded micelle enhances the alleviation of intervertebral disc degeneration by adipose-derived stem cell, Bioact. Mater. 6 (10) (2021) 3568–3579.

[21] H. Chen, Y. Fu, K. Feng, Y. Zhou, X. Wang, H. Huang, Y. Chen, W. Wang, Y. Xu, H. Tian, Y. Mao, J. Wang, Z. Zhang, Polydopamine-coated UiO-66 nanoparticles loaded with perfluorotributylamine/tirapazamine for hypoxia-activated osteosarcoma therapy, J. Nanobiotechnol. 19 (1) (2021) 298.

[22] Z. Zhou, B. Zhang, S. Wang, W. Zai, A. Yuan, Y. Hu, J. Wu, Perfluorocarbon nanoparticles mediated platelet blocking disrupt vascular barriers to improve the efficacy of oxygen-sensitive antitumor drugs, Small 14 (45) (2018), e1801694.

[23] A.B. Allen, J.A. Zimmermann, O.A. Burnsed, D.C. Yakubovich, H.Y. Stevens, Z. Gazit, T.C. McDevitt, R.E. Guldberg, Environmental manipulation to promote stem cell survival in vivo: use of aggregation, oxygen carrier, and BMP-2 co-delivery strategies, J. Mater. Chem. B 4 (20) (2016) 3594–3607.

[24] T. Ma, Y. Wang, F. Qi, S. Zhu, L. Huang, Z. Liu, J. Huang, Z. Luo, The effect of synthetic oxygen carrier-enriched fibrin hydrogel on Schwann cells under hypoxia condition in vitro, Biomaterials 34 (38) (2013) 10016–10027.

[25] Y. Wang, F. Qi, S. Zhu, Z. Ye, T. Ma, X. Hu, J. Huang, Z. Luo, A synthetic oxygen carrier in fibrin matrices promotes sciatic nerve regeneration in rats, Acta Biomater. 9 (7) (2013) 7248–7263.

[26] Z. Sun, B. Luo, Z. Liu, L. Huang, B. Liu, T. Ma, B. Gao, Z.H. Liu, Y.F. Chen, J.H. Huang, Z. Luo, Effect of perfluorotributylamine-enriched alginate on nucleus pulposus cell: implications for intervertebral disc regeneration, Biomaterials 82 (2016) 34–47.

[27] X. Li, Q. Dou, Q. Kong, Repair and regenerative therapies of the annulus fibrosus of the intervertebral disc, J. Coll. Phys. Surg. Pak. 26 (2) (2016) 138–144.

[28] C. Li, J. Chen, Y. Lv, Y. Liu, Q. Guo, J. Wang, C. Wang, P. Hu, Y. Liu, Recent progress in electrospun nanofiber-based degenerated intervertebral disc repair, ACS Biomater. Sci. Eng. 8 (1) (2022) 16–31.

[29] M. Gluais, J. Clouet, M. Fusellier, C. Decante, C. Moraru, M. Dutilleul, J. Veziers, J. Lesoeur, D. Dumas, J. Abadie, A. Hamel, E. Bord, S.Y. Chew, J. Guicheux, C. Le Visage, In vitro and in vivo evaluation of an electrospun-aligned microfibrous implant for Annulus fibrosus repair, Biomaterials 205 (2019) 81–93.

[30] R. Kang, H. Li, Z. Xi, S. Ringgard, A. Baatrup, K. Rickers, M. Sun, D.Q.S. Le, M. Wang, L. Xie, Y. Xie, M. Chen, C. Bünger, Surgical repair of annulus defect with biomimetic multilamellar nano/microfibrous scaffold in a porcine model, J. Tissue Eng. Regen Med. 12 (1) (2018) 164–174.

[31] Q. Yu, F. Han, Z. Yuan, Z. Zhu, C. Liu, Z. Tu, Q. Guo, R. Zhao, W. Zhang, H. Wang, H. Mao, B. Li, C. Zhu, Fucoidan-loaded nanofibrous scaffolds promote annulus fibrosus repair by ameliorating the inflammatory and oxidative microenvironments in degenerative intervertebral discs, Acta Biomater. 148 (2022) 73–89.

[32] G. Chu, Z. Yuan, C. Zhu, P. Zhou, H. Wang, W. Zhang, Y. Cai, X. Zhu, H. Yang, B. Li, Substrate stiffness- and topography-dependent differentiation of annulus fibrosus-derived stem cells is regulated by Yes-associated protein, Acta Biomater. 92 (2019) 254–264.

[33] T. Ma, Y. Yang, X. Quan, L. Lu, B. Xia, J. Gao, F. Qi, S. Li, L. Zhao, L. Mei, Y. Zheng, Y. Shen, Z. Luo, Y. Jin, J. Huang, Oxygen carrier in core-shell fibers synthesized by coaxial electrospinning enhances Schwann cell survival and nerve regeneration, Theranostics 10 (20) (2020) 8957–8973.

[34] Y. Han, F. Yuan, C. Deng, F. He, Y. Zhang, H. Shen, Z. Chen, L. Qian, Metformin decreases LPS-induced inflammatory response in rabbit annulus fibrosus stem/progenitor cells by blocking HMGB1 release, Aging (Albany NY) 11 (22) (2019) 10252–10265.

[35] C. Zhu, J. Li, C. Liu, P. Zhou, H. Yang, B. Li, Modulation of the gene expression of annulus fibrosus-derived stem cells using poly(ether carbonate urethane)urea scaffolds of tunable elasticity, Acta Biomater. 29 (2016) 228–238.

[36] Y. Zheng, Y. Hao, B. Xia, L. Mei, S. Li, X. Gao, T. Ma, B. Wei, Z. Tan, P. Lan, Z. Luo, D. Jing, J. Huang, Circadian rhythm modulates the therapeutic activity of pulsed electromagnetic fields on intervertebral disc degeneration in rats, Oxid. Med. Cell. Longev. 2022 (2022), 9067611.

[37] Y. Zheng, L. Mei, S. Li, T. Ma, B. Xia, Y. Hao, X. Gao, B. Wei, Y. Wei, D. Jing, Z. Luo, J. Huang, Pulsed electromagnetic field alleviates intervertebral disc degeneration by activating sirt1-autophagy signaling network, Front. Bioeng. Biotechnol. 10 (2022), 853872.

[38] Q. Guo, C. Liu, J. Li, C. Zhu, H. Yang, B. Li, Gene expression modulation in TGF-β3-mediated rabbit bone marrow stem cells using electrospun scaffolds of various stiffness, J. Cell Mol. Med. 19 (7) (2015) 1582–1592.

[39] H. Wang, D. Wang, B. Luo, D. Wang, H. Jia, P. Peng, Q. Shang, J. Mao, C. Gao, Y. Peng, L. Gan, J. Du, Z. Luo, L. Yang, Decoding the annulus fibrosus cell atlas by scRNA-seq to develop an inducible composite hydrogel: a novel strategy for disc reconstruction, Bioact. Mater. 14 (2022) 350–363.

[40] N.S. Aziz, N. Yusop, A. Ahmad, Importance of stem cell migration and angiogenesis study for regenerative cell-based therapy: a review, Curr. Stem Cell Res. Ther. 15 (3) (2020) 284–299.

[41] J. Piñeiro-Llanes, S. Suzuki-Hatano, A. Jain, V.A. Pérez Medina, W.T. Cade, C.A. Pacak, C.S. Simmons, Matrix produced by diseased cardiac fibroblasts affects early myotube formation and function, Acta Biomater. 152 (2022) 100–112.

[42] C. Liu, Z. Jin, X. Ge, Y. Zhang, H. Xu, Decellularized annulus fibrosus matrix/chitosan hybrid hydrogels with basic fibroblast growth factor for annulus fibrosus tissue engineering, Tissue Eng. Part A 25 (23–24) (2019) 1605–1613.

[43] Y. Ahn, Endoscopic spine discectomy: indications and outcomes, Int. Orthop. 43 (4) (2019) 909–916.

[44] H.Y. Yoo, S.J. Kim, Oxygen-dependent regulation of ion channels: acute responses, post-translational modification, and response to chronic hypoxia, Pflügers Archiv 473 (10) (2021) 1589–1602.

[45] J. Lopez-Barneo, R. Pardal, P. Ortega-Sáenz, Cellular mechanism of oxygen sensing, Annu. Rev. Physiol. 63 (2001) 259–287.

[46] L. Eaton, M.E. Pamenter, What to do with low O(2): redox adaptations in vertebrates native to hypoxic environments, Comp. Biochem. Physiol. Mol. Integr. Physiol. 271 (2022), 111259.

[47] H.L. Haller, F. Sander, D. Popp, M. Rapp, B. Hartmann, M. Demircan, S.P. Nischwitz, L.P. Kamolz, Oxygen, pH, lactate, and metabolism-how old knowledge and new insights might Be combined for new wound treatment, Medicina (Kaunas) 57 (11) (2021).

[48] B. Huang, M. Chen, J. Tian, Y. Zhang, Z. Dai, J. Li, W. Zhang, Oxygen-carrying and antibacterial fluorinated nano-hydroxyapatite incorporated hydrogels for enhanced bone regeneration, Adv. Healthc. Mater 11 (12) (2022), e2102540.

[49] S.J. Lin, C.C. Huang, Strontium peroxide-loaded composite scaffolds capable of generating oxygen and modulating behaviors of osteoblasts and osteoclasts, Int. J. Mol. Sci. 23 (11) (2022).

[50] L. Liu, J. Wan, M. Dai, X. Ye, C. Liu, C. Tang, L. Zhu, Effects of oxygen generating scaffolds on cell survival and functional recovery following acute spinal cord injury in rats, J. Mater. Sci. Mater. Med. 31 (12) (2020) 115.

[51] Z. Li, X. Guo, J. Guan, An oxygen release system to augment cardiac progenitor cell survival and differentiation under hypoxic condition, Biomaterials 33 (25) (2012) 5914–5923.

[52] T. Agarwal, S. Kazemi, M. Costantini, F. Perfeito, C.R. Correia, V. Gaspar, L. Montazeri, C. De Maria, J.F. Mano, M. Vosough, P. Makvandi, T.K. Maiti, Oxygen releasing materials: towards addressing the hypoxia-related issues in tissue engineering, Mater Sci. Eng. C Mater Biol. Appl. 122 (2021), 111896.

[53] A. Erdem, R. Haghniaz, Y.N. Ertas, S.K. Sangabathuni, A.S. Nasr, W. Swieszkowski, N. Ashammakhi, Methods for fabricating oxygen releasing biomaterials, J. Drug Target. 30 (2) (2022) 188–199.
[54] N.G.A. Willemen, S. Hassan, M. Gurian, M.F. Jasso-Salazar, K. Fan, H. Wang, M. Becker, I.E. Allijn, A. Bal-Öztürk, J. Leijten, S.R. Shin, Enzyme-Mediated alleviation of peroxide toxicity in self-oxygenating biomaterials, Adv. Healthc. Mater 11 (13) (2022), e2102697.
[55] A.L. Farris, D. Lambrechts, Y. Zhou, N.Y. Zhang, N. Sarkar, M.C. Moorer, A.N. Rindone, E.L. Nyberg, A. Perdomo-Pantoja, S.J. Burris, K. Free, T.F. Witham, R.C. Riddle, W.L. Grayson, 3D-printed oxygen-releasing scaffolds improve bone regeneration in mice, Biomaterials 280 (2022), 121318.
[56] C. Haltern, U.P. Siekmann, A.F. Rump, R. Rossaint, [Hyperbaric oxygen therapy (HBO): current standing], Anasthesiol Intensivmed Notfallmed Schmerzther 35 (8) (2000) 487–502.
[57] M. Heyboer 3rd, D. Sharma, W. Santiago, N. McCulloch, Hyperbaric oxygen therapy: side effects defined and quantified, Adv. Wound Care 6 (6) (2017) 210–224.
[58] P.A. Shiekh, A. Singh, A. Kumar, Oxygen-releasing antioxidant cryogel scaffolds with sustained oxygen delivery for tissue engineering applications, ACS Appl. Mater. Interfaces 10 (22) (2018) 18458–18469.
[59] J. Li, Y. Liu, H.E. Abdelhakim, Drug delivery applications of coaxial electrospun nanofibres in cancer therapy, Molecules 27 (6) (2022).
[60] F. Mohammadian, A. Eatemadi, Drug loading and delivery using nanofibers scaffolds, Artif. Cell Nanomed. Biotechnol. 45 (5) (2017) 881–888.
[61] G. Chu, C. Shi, H. Wang, W. Zhang, H. Yang, B. Li, Strategies for annulus fibrosus regeneration: from biological therapies to tissue engineering, Front. Bioeng. Biotechnol. 6 (2018) 90.
[62] A.P. Peredo, S.E. Gullbrand, H.E. Smith, R.L. Mauck, Putting the pieces in place: mobilizing cellular players to improve annulus fibrosus repair, Tissue Eng. B Rev. 27 (4) (2021) 295–312.
[63] C. Liu, Q. Guo, J. Li, S. Wang, Y. Wang, B. Li, H. Yang, Identification of rabbit annulus fibrosus-derived stem cells, PLoS One 9 (9) (2014), e108239.
[64] J.N. Wei, F. Cai, F. Wang, X.T. Wu, L. Liu, X. Hong, W.H. Tang, Transplantation of CXCR4 overexpressed mesenchymal stem cells augments regeneration in degenerated intervertebral discs, DNA Cell Biol. 35 (5) (2016) 241–248.
[65] Z. Zhou, S. Zeiter, T. Schmid, D. Sakai, J.C. Iatridis, G. Zhou, R.G. Richards, M. Alini, S. Grad, Z. Li, Effect of the CCL5-releasing fibrin gel for intervertebral disc regeneration, Cartilage 11 (2) (2020) 169–180.
[66] H. Zhang, S. Yu, X. Zhao, Z. Mao, C. Gao, Stromal cell-derived factor-1α-encapsulated albumin/heparin nanoparticles for induced stem cell migration and intervertebral disc regeneration in vivo, Acta Biomater. 72 (2018) 217–227.
[67] D.M. Elliott, L.A. Setton, Anisotropic and inhomogeneous tensile behavior of the human anulus fibrosus: experimental measurement and material model predictions, J. Biomech. Eng. 123 (3) (2001) 256–263.
[68] G.D. O'Connell, H.L. Guerin, D.M. Elliott, Theoretical and uniaxial experimental evaluation of human annulus fibrosus degeneration, J. Biomech. Eng. 131 (11) (2009), 111007.
[69] J.P. Corredor-Gómez, A.M. Rueda-Ramírez, M.A. Gamboa-Márquez, C. Torres-Rodríguez, C.J. Cortés-Rodríguez, An intramembranous ossification model for the in silico analysis of bone tissue formation in tooth extraction sites, J. Theor. Biol. 401 (2016) 64–77.
[70] Q. Ding, S.J. Liao, J. Yu, Axon guidance factor netrin-1 and its receptors regulate angiogenesis after cerebral ischemia, Neurosci. Bull. 30 (4) (2014) 683–691.
[71] J. Huang, Q. Han, M. Cai, J. Zhu, L. Li, L. Yu, Z. Wang, G. Fan, Y. Zhu, J. Lu, G. Zhou, Effect of angiogenesis in bone tissue engineering, Ann. Biomed. Eng. 50 (8) (2022) 898–913.